

Quasi-static strain governing ultrafast spin dynamics

Yooleemi Shin^{1,2}, Mircea Vomir³, Dong-Hyun Kim², Phuoc Cao Van⁴, Jong-Ryul Jeong⁴ ⁴ & Ji-Wan Kim¹ ¹✉

The quasi-static strain (QSS) is the product induced by the lattice thermal expansion after ultrafast photo-excitation. Although the ultrafast spin dynamics driven by the QSS and thermal effects are barely distinguishable in time, they should be treated separately because of their different fundamental actions. By employing ultrafast Sagnac interferometry and the magneto-optical Kerr effect, we demonstrate quantitatively the existence of QSS and the decoupling of two effects counteracting each other in typical polycrystalline Co and Ni films. The Landau-Lifshitz-Gilbert and Kittel equations considering a magnetoelastic energy term showed that QSS, rather than the thermal energy, in ferromagnets plays a governing role in ultrafast spin dynamics. This demonstration provides a way to analyze ultrafast photo-induced phenomena.

¹Department of Physics, Kunsan National University, Kunsan 54150, South Korea. ²Department of Physics, Chungbuk National University, Cheongju 28644, South Korea. ³Université de Strasbourg, CNRS, Institut de Physique et Chimie des Matériaux de Strasbourg, UMR 7504, 67034 Strasbourg, France. ⁴Department of Materials Science and Engineering, Chungnam National University, Daejeon 34134, South Korea. ✉email: hwoarang@kunsan.ac.kr

Magnetoelasticity, which is the coupling of spin and strain, is a universal phenomenon in magnetic materials and enables active control of the spin states by modifying the material dimensions¹. Thus far, it has been investigated that the spin dynamics after ultrafast spin angular momentum transfer by photo-excitation^{2–7} is governed by time-dependent effective fields with origins such as magnetocrystalline⁸, dipole, Zeeman⁹, exchange^{10–12}, terahertz^{13,14}, magnetoelasticity^{15,16}, and spin current^{17–19}. These have been described mainly by electron and spin degrees of freedoms, while the lattice degree of freedom was highlighted only recently²⁰.

The increase in lattice temperature by photo-excitation generates two types of strain, which are the propagating strain $\eta_p(z, t)$ with a few-ps temporal width and the quasi-static strain (QSS: $\eta_{qss}(t)$) at a penetration length scale with a heat dissipation time. In the recent decade, the interaction of spins with η_p has attracted considerable research attention from diverse points of view^{15,16,21–23}. On the other hand, QSS has not been a major focus despite its comparable amplitude to that of η_p . As principal reasons, the QSS and thermal dependence of materials are inextricable, particularly in photo-induced experiments. Moreover, the QSS is difficult to quantify only with a differential reflectivity that is typical measurement data in a pump–probe experiment. Therefore, great care must be taken in determining $\eta_{qss}(t)$. In general, the three temperatures model is used to extract the time-dependent temperature information of the sub-systems by fitting with the experimental curves of spin and reflectivity dynamics. These temperature profiles can account for the only temperature contribution to the reflectivity, not the strain contribution. This might deliver improper messages and hinder unveiling the new physics of ultrafast dynamics. The earlier work describes the contributions of the QSS and thermal effects to the spin dynamics of a galfenol film depending on the external magnetic field strength²⁴. In addition, for an integrated understanding, the experimental quantification of the QSS and its competition with the thermal effect by various experimental conditions remain to be proven. As the QSS and the thermal effects have different contributions to dynamics (the former changes the plasmonic²⁵ or electronic bands²⁶ and the latter changes the electron populations), systematic and comprehensive measurement approaches to separate the two effects are required for the complete analysis of the fundamental mechanism of the ultrafast photo-induced spin dynamics.

Using ultrafast Sagnac interferometry (USI) and a magneto-optical Kerr effect (MOKE) instrument, we demonstrate in this work that the QSS in ferromagnetic films governs the ultrafast spin dynamics from the first ps to the ns timescale. In particular, USI is used to prove the existence of QSS by measuring the lattice expansion dynamics directly. Here, three important sets of evidence that could not be explained by the thermal effect are as follows: (i) the increase in spin precession frequency with the pump intensity, (ii) π -phase inversion of the precession, and (iii) the pronounced background distinguished from incoherent phonons and magnons. The model calculation of the Landau–Lifshitz–Gilbert (LLG) equation incorporating the time-dependent QSS strongly supports that all features mentioned are elucidated by one concept of QSS. The scenario is consolidated with full consistency using other ferromagnets (Co, Ni, and Ni_xFe_{1-x}) to adjust the competition between strain and thermal effects.

Results

Experimental configurations of MOKE and USI measurements.

The measurement geometries are shown in Fig. 1a. The bilayer structure of Al₂O₃(5 nm)/Co(25 nm)/Al₂O₃(substrate) and the trilayer structure of Co(200 nm)/Al₂O₃(15 nm)/Co(25 nm)/

Al₂O₃(substrate) were prepared by magnetron sputtering (nm in thickness are omitted hereafter). The Al₂O₃(5) layer in the bilayer structure was deposited to prevent oxidation. In the trilayer structure, the Al₂O₃(15) was used both to suppress the possible propagation of thermal magnons from the top Co layer and to match acoustic impedance with Co. The acoustic impedance Z is given by a product of mass density χ and sound velocity v . The acoustic reflection coefficient $r_{ac} = (Z_{Co} - Z_{Al_2O_3}) / (Z_{Co} + Z_{Al_2O_3})$ between Co and Al₂O₃ with $\chi_{Co} = 8.9 \times 10^3 \text{ kg m}^{-3}$, $v_{Co} \sim 5.8 \text{ km s}^{-1}$ ²⁷ and $\chi_{Al_2O_3} = 3.98 \times 10^3 \text{ kg m}^{-3}$, $v_{Al_2O_3} \sim 11.2 \text{ km s}^{-1}$ ²⁸ is ~ 0.07 showing the good impedance matching.

For MOKE measurements, we used Ti:sapphire regenerative amplified laser pulses with a repetition rate of 10 kHz, a temporal width of 40 fs, and a center wavelength of 800 nm (The details of the MOKE setup are given in Methods). The frequency-doubled pump pulses ($\lambda_{pu} = 400 \text{ nm}$) excite the front sides of samples and probe pulses ($\lambda_{pr} = 800 \text{ nm}$) measure the differential Kerr rotation $\Delta\theta(t)$ and reflectivity $\Delta R(t)$ either of the front side for the bilayer or the back side for the trilayer, as shown in Fig. 1a-I, a-II, respectively. The strain pulse generated in the Co(200) surface in the trilayer propagates and triggers the spin precession in Co(25) layer through magnetoelastic coupling. For USI measurement, the front pump–front probe geometry we first tried partially degrades the quality of probe polarization. Therefore, in the current experiment, we make the pump pulses excite the back side of Co, and the probe pulses measure the front side (Fig. 1a-III). In Fig. 1b, we present the simulated strain profiles $\eta(z, t)$ at $t = 7$ (blue) and 20 ps (green) for the top Co layer in the trilayer structure for a better understanding of the time evolution of $\eta_p(z)$ propagating into the film depth and $\eta_{qss}(z)$ bidding at a penetration length scale. For simplicity, we used $\eta_{qss}(t) = \eta(0, t)$ hereafter.

The main purpose of USI²⁹ is to measure unambiguously the lattice displacement dynamics $u(z=0, t)$ and extract $\eta_{qss}(t) = \partial u(z, t) / \partial z|_{z=0}$ in the end. The USI was built with a Ti:sapphire oscillator system operating at a repetition rate of 80 MHz, a temporal width of 40 fs, and a center wavelength of 800 nm. To avoid possible heat accumulation by a prepulse, the repetition rate is lowered down to 1 MHz by an electro-optic modulator (see “Methods” and Supplementary Note 1 for more details of the USI instrument). We confirmed that all data measured here have no heat accumulation from a prepulse by assuring zero background offset. Although $\Delta R(t)$ resulted from a change in a complex refractive index \tilde{n} is linked to $\eta(z, t)$ through the relation $\Delta\tilde{n} = (\partial\tilde{n}/\partial T)\Delta T + (\partial\tilde{n}/\partial\eta)\Delta\eta$, it is relatively difficult to extract $\eta(z, t)$ directly because of an unknown piezo-optic property ($\partial\tilde{n}/\partial\eta$) of materials except for Ni, Cr, and Au at specified wavelengths^{30,31}. Instead, as a circumvention, $\eta_{qss}(t)$ was obtained without introducing unknown coefficients by solving the one-dimensional wave equation incorporating the lattice temperature profile used as a driving source (see the strain calculation and parameter values in “Methods” for more details). The lattice temperature profile was calculated using a three temperatures model with proper parameter values of a bulk Co. In addition, the pump intensity calibration between the two different instruments (MOKE and USI) was performed by matching their signal levels of $\Delta R(t)/R$. Figure 1c shows the real part of the Sagnac signal $\rho = \Delta R/2R$ (Fig. 1c-I) and the converted lattice displacement $u(0, t) = \lambda_{pr}\delta\phi/4\pi$ (Fig. 1c-II) from the imaginary part ($\delta\phi$) of $\delta r/r \sim \rho + i\delta\phi$ for the bilayer structure (blue circles for the measurement and the yellow line for the reproduction from the calculation). Here, r is defined as the complex amplitude-reflection coefficient of the sample, ρ the relative change in reflectance, and $\delta\phi$ the phase change induced by the pump pulse. In principle, $\eta_{qss}(t)$ can be obtained from the relation

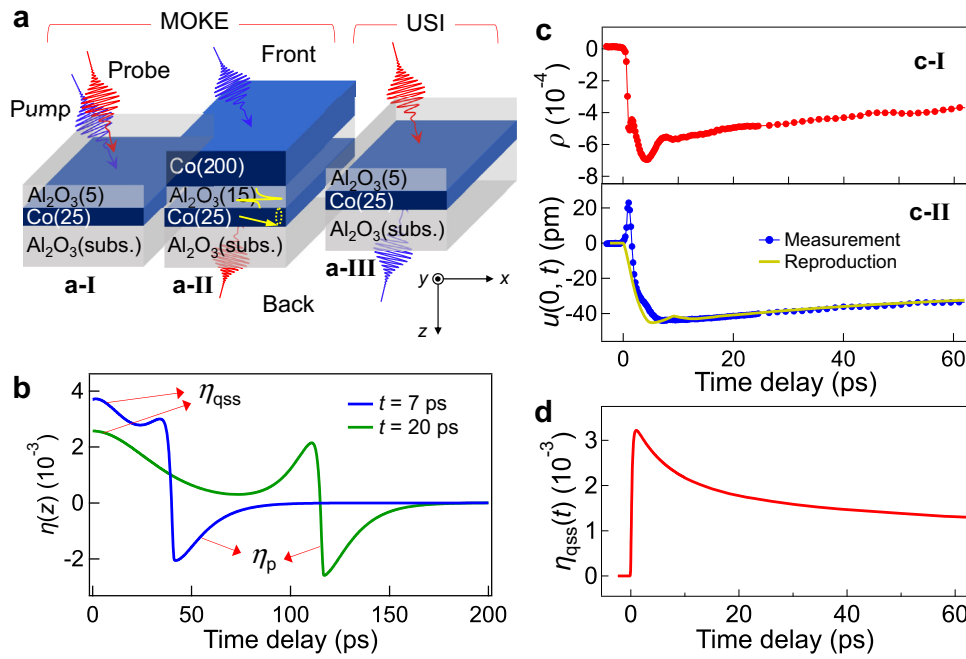


Fig. 1 Measurement geometry and ultrafast Sagnac interferometric data. **a** Simple images of the pump–probe magneto-optical Kerr effect (MOKE) and ultrafast Sagnac interferometry (USI) measurements. For MOKE, the front-pump and front-probe for the bilayer (**a-I**), the front-pump and back-probe schemes for the trilayer (**a-II**) were used. The back-pump and front-probe for the bilayer (**a-III**) were used for the Sagnac measurements. **b** Dynamic strain pulse profiles $\eta(z, t)$ calculated for the top Co layer in the trilayer structure at $t = 7$ ps (blue curve) and 20 ps (green curve): the propagating bipolar pulse $\eta_p(z)$ and the quasi-static strain $\eta_{qss}(z)$. **c** Sagnac interferometric curves for Co bilayer: $\rho = \Delta R / 2R$ (**c-I**: ρ —relative change in reflectance induced by the pump pulse and ΔR —differential reflectivity) and the lattice displacement $u(0, t)$ (**c-II**: experimental data (blue circles) and reproduced one by calculation (yellow line)). **d** $\eta_{qss}(t)$ profile extracted from the reproduced data $u(0, t)$.

$\eta(z, t) = \partial u(z, t) / \partial z$. However, as $u(0, t)$ measured from USI is only one particular case of $u(z, t)$, it is not possible to directly obtain $\eta_{qss}(t) = \partial u(z, t) / \partial z|_{z=0}$. To bypass this problem, we first obtain a trial solution $u(z, t)$ by calculating the wave equation combined with the three temperature models (see “Methods”). Then, by iteratively adjusting the pump intensity parameter and unknown heat coupling coefficients g_{ij} , we find the final solution $u(z, t)$ that best matches $u(0, t)$ to the experimental curve measured by USI. Now that $u(z, t)$ is known based on the measurement quantity, $\eta_{qss}(t)$ can be reproduced as shown in Fig. 1d. The positive value of η_{qss} stands for a tensile strain resulted from the lattice expansion by a sign convention.

In contrast to the reproduced yellow curve in Fig. 1c-II, the experimental data $u(0, t)$ shows a sharp positive peak at the first ps, indicating lattice contraction into the film direction. This may be explained by several possible candidates, such as the electronic stress by photo-excitation³² and the magnetic stress driven by ultrafast demagnetization in FePt nanogranular structures^{33–35}. However, the continuous film case in ref. 35 showed that the compressive strain was not produced due to the in-plane constraints upon the lattice expansion. This is a different result from our experimental data $u(0, t)$ shown in Fig. 1c-II. However, identifying the origin is beyond the current scope of this paper, and the lattice contraction has not been considered in the reproduction process.

Variation of spin precession frequency as a function of pump intensity. The solid circles in Fig. 2a show $\Delta\theta(t)$ of the Co bilayer under the magnetic field $H_{\text{ext}} = 0.4$ T and $\varphi = 60^\circ$ (φ : the magnetic field angle from out-of-plane direction) with various pump intensities I_p . The experimental curves for other field angles ($\varphi = 15, 30$, and 45°) are presented in Supplementary Note 2. The precession frequency f was obtained by fitting the experimental

curves with the following damped sinusoidal function:

$$\Delta\theta(t) = A \exp\left(-\frac{t}{\tau_1}\right) \sin(2\pi ft + \delta_0) + B \exp\left(-\frac{t}{\tau_2}\right) + C \quad (1)$$

where τ_1 is the spin relaxation time, τ_2 the decay time of the background signal, δ_0 the initial phase of the precession, A and B the amplitudes of the first two terms on the right-hand side, and C defined as the background offset. The solid line in Fig. 2a denotes the fit curve for the highest I_p . Figure 2b shows that the change in the precession frequency ($\Delta f / f_m = (f - f_m) / f_m$) increases with I_p for all magnetic field angles ($\varphi = 15^\circ$: black, 30° : red, 45° : green, 60° : blue circles). The error bars are marked on the data points). Here, f_m is defined as the precession frequency for the minimum I_p and corresponds to 13.8, 20.0, 24.4, and 27.6 GHz for the respective angles of φ (15, 30, 45, and 60°). This frequency variation observed for the polycrystalline Co film has an opposite trend to what would be expected from the conventional magnetic energy terms such as the magneto-crystalline, dipolar, and Zeeman energy. The magnitude of the effective magnetic field $H_{\text{eff}}(t)$ in such case would decrease with the increasing temperature of the sub-systems or the increasing I_p .

In order to figure out the effect of $\eta_{qss}(t)$ on the precession frequency f , we solved the following LLG equation.

$$\frac{d\mathbf{M}}{dt} = -\gamma_s \mu_0 (\mathbf{M} \times \mathbf{H}_{\text{eff}}) + \frac{\alpha_d}{M_s} \left(\mathbf{M} \times \frac{d\mathbf{M}}{dt} \right) \quad (2)$$

where M_s is the saturation magnetization, \mathbf{H}_{eff} the effective magnetic field vector defined as $\mathbf{H}_{\text{eff}} = -\partial F_{\text{tot}} / \mu_0 \partial \mathbf{M}$, $\gamma_s = 1.63 \times 10^{11} \text{ rad s}^{-1} \text{ T}^{-1}$ the gyromagnetic ratio³⁶, and the phenomenological damping constant $\alpha_d = 0.015$ is assumed. The total magnetic free energy (F_{tot}) consists of the magnetocrystalline, dipole, Zeeman, and the magnetoelastic energy terms as

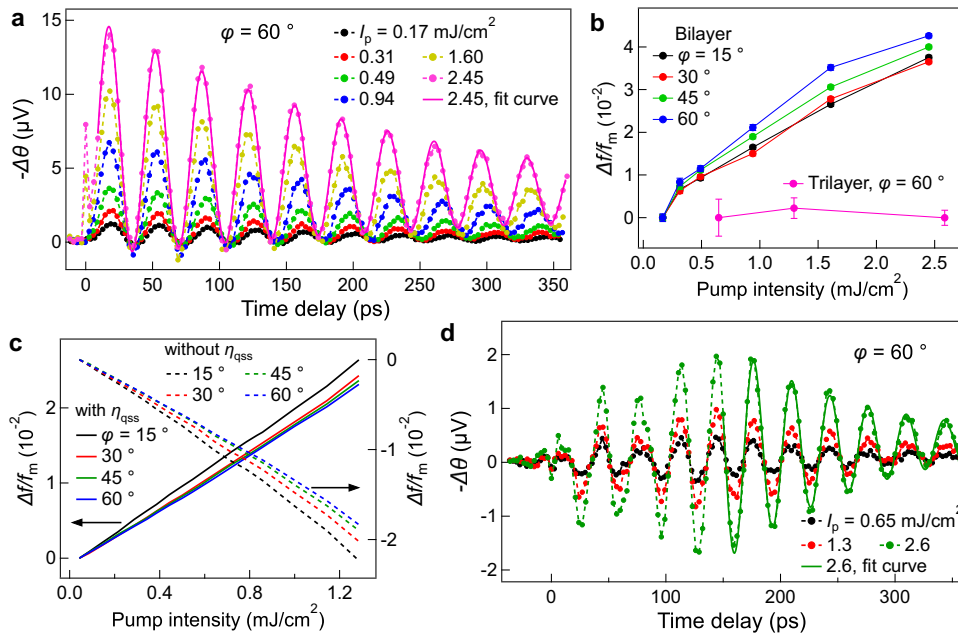


Fig. 2 Spin precession as a function of the pump intensity of the Co bilayer. **a** Differential magneto-optical Kerr rotations $\Delta\theta(t)$ of the Co(25) bilayer as a function of pump intensity I_p under the magnetic field $H_{\text{ext}} = 0.4$ T and $\varphi = 60^\circ$ (φ : the magnetic field angle from out-of-plane direction). **b** Summary of the frequency change of the spin precession $\Delta f/f_m$ for the bilayer as a function of I_p and φ (15° : black, 30° : red, 45° : green, 60° : blue circles). Here f_m is defined as the precession frequency for the minimum I_p . The pink circles present $\Delta f/f_m$ obtained from the Co(25) in the trilayer. All data points are presented with error bars obtained from the least-square fit. **c** Model calculation results of $\Delta f/f_m$ based on the Landau-Lifshitz-Gilbert (LLG) equation for the presence (solid lines) and absence (dashed lines) of η_{qss} , respectively. **d** $\Delta\theta(t)$ induced by η_p for the trilayer under $H_{\text{ext}} = 0.4$ T and $\varphi = 60^\circ$.

follows:

$$F_{\text{tot}} = K_u(M)\sin^2\vartheta + \frac{1}{2}\mu_0 \sum_i N_i M_i^2(t) - \mu_0 \sum_i M_i(t)H_{\text{ext},i} - \frac{3}{2}\lambda_s \sigma_s \cos^2\vartheta \quad (3)$$

For the polycrystalline Co film, we used following parameter values: uniaxial magnetic anisotropy coefficient $K_u \sim 0$, the magnetostriction value $\lambda_s = -62 \mu^{37}$ the mechanical stress $\sigma_s = 3(1 + \nu)(1 - \nu)^{-1} B \eta_{\text{qss}}(t)$, Poisson's ratio $\nu = 0.31$, the bulk modulus $B = 190$ GPa²⁷, and the demagnetizing factor $N_x = N_y = 0$, $N_z = 1$. ϑ is defined as the angle between the magnetization \mathbf{M} and σ_s (out-of-plane) direction. From the time-dependent profiles of $K_u(t)$, $M(t)$, $\eta_{\text{qss}}(t)$, and $\vartheta(t)$ calculated after solving both the three temperatures model and the wave equation based on the measurement curve $u(t)$, the magnetization dynamics $d\mathbf{M}/dt$ is obtained (see “Methods” for calculation details about the three temperatures model and the wave equation).

After calculating the spin precession and extracting f from $d\mathbf{M}/dt$, the simulation results are summarized in Fig. 2c. The values of $\Delta f/f_m$ considering $\eta_{\text{qss}}(t)$ (solid lines, on the left axis) are in good agreement with experimental data of Fig. 2b, showing an increase in $\Delta f/f_m$ up to 2% for a wide range of φ . In contrast, for the absence of $\eta_{\text{qss}}(t)$, $\Delta f/f_m$ decreased by 1.6% (dashed lines, on the right axis), as expected with conventional energy terms. We also checked the case when the spin precession was involved in neither thermal nor QSS effects. This requirement was met by the back-side measurement of the trilayer structure. The strain pulse $\eta_p(z, t)$ generated from the Co top layer propagates to the Co underlayer without carrying the thermal energy and contributes only to triggering spin precession through magnetoelastic coupling. From $\Delta\theta(t)$ with a function of I_p under $\varphi = 60^\circ$ in Fig. 2d (the fit curve with Eq. (1) for the highest I_p is denoted by the solid line), $\Delta f/f_m$ did not show a noticeable change within the experimental uncertainty (see the pink curve in Fig. 2b). Here

$I_p = 2.6$ mJ cm⁻² corresponds to ~70% of the burning threshold for the Co top layer.

Ferromagnetic resonance frequency dependence on T , φ , and η_{qss} . To obtain the comprehensive picture of the QSS effect on f over a wide range of temperature T and field angle φ , the ferromagnetic resonance frequency f_r was calculated using the classical Kittel equation with the magnetic free energy F , as used in the dynamics case.

$$f_r = \gamma_s \frac{(F_{\text{cs}} F_{\xi\xi} - F_{\xi\xi}^2)^{1/2}}{2\pi M(T) \sin \zeta_{\text{eq}}}, \quad (4)$$

where $F_{pq} = \partial^2 F / \partial p \partial q$. The symbols ζ and ξ denote the polar and azimuthal angles in a spherical coordinate system, respectively. ζ_{eq} is defined as the equilibrium angle of magnetization, and $\xi = \pi/2$ is set due to the azimuthal symmetry of the sample. As the classical Kittel equation generally treats the static regime, the QSS is assumed to be a constant supposing no thermal relaxation after a thermal equilibrium among the sub-systems. Hence, the QSS can be handled simply with thermal strain $\eta_{\text{th}}(T) = \beta \Delta T$ (thermal expansion coefficient of Co²⁷: $\beta = 13.7 \mu$). Figure 3a, b present the contour map of f_r with the control parameters of T (x -axis) and φ (y -axis) under $H_{\text{ext}} = 0.4$ T for the absence and presence of $\eta_{\text{th}}(T)$, respectively. Figure 3a shows that f_r decreases monotonically with increasing T at a fixed value of φ (along the yellow line). In contrast, Fig. 3b indicates that f_r increases gently with T up to ~800 K (blue box region). This is because $\eta_{\text{th}}(T)$ increases almost linearly with T , unlike the barely altered $M(T)$ owing to its high Curie temperature T_c . Hence, the effect of magnetoelasticity plays a dominant role over those of the conventional magnetic energy terms. At a higher T (orange box region), the rapid drop of $M(T)$ reduces the effective field strength, leading to the inflection point of f_r around 800 K.

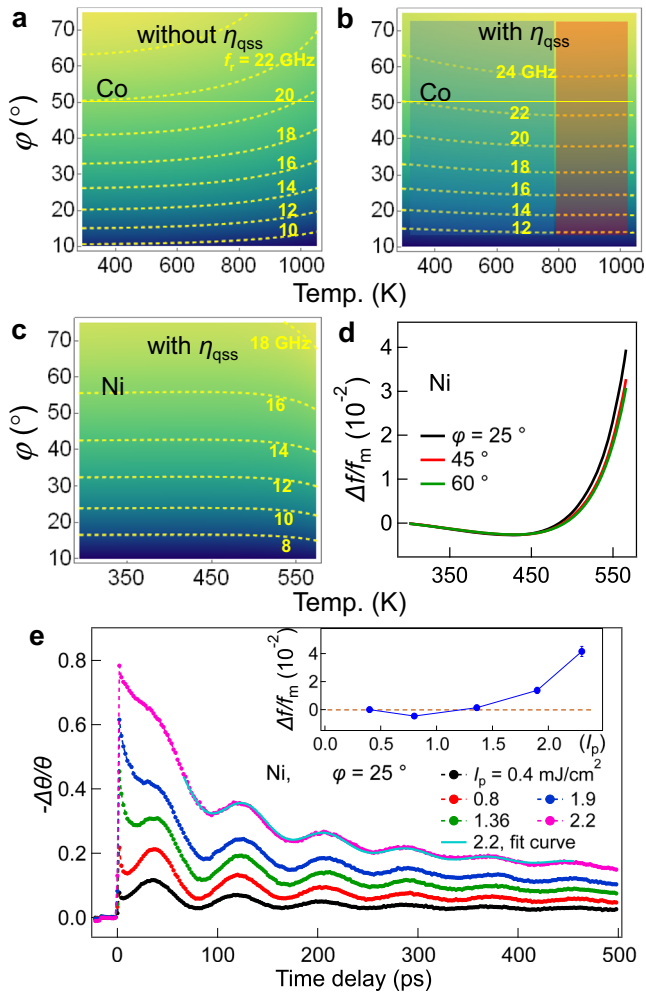


Fig. 3 Ferromagnetic resonance frequency with the control parameters T , φ , and η_{QSS} . Contour maps of a ferromagnetic resonance frequency f_r calculated using the classical Kittel equation as a function of temperature T and magnetic field angle φ under $H_{\text{ext}} = 0.4$ T, for the absence (a for Co) and presence (b for Co and c for Ni) of η_{QSS} , respectively. The f_r decreases monotonically with increasing T for case a, but increases moderately showing the inflection point around 800 K for case b, implying competition between the thermal and strain effects. The shaded boxes in b stand for the domains where f_r increases (blue) and starts to slow down (red) as T increases. d Selected curves of $\Delta f/f_m$ at $\varphi = 25, 45$, and 60° from c. e $\Delta\theta(t)/\theta$ of Ni(270)/SiO₂ under $H_{\text{ext}} = 0.4$ T and $\varphi = 25^\circ$ as a function of I_p . Unlike the Co bilayer, the sign of $\Delta f/f_m$ changes, as shown in the inset, confirming the competition between the thermal and the quasi-static strain (QSS) effects. All data points in the inset are presented with error bars obtained from the least-square fit.

This is not a special case only for Co but can be generalized to a broad class of magnetoelastic materials. We can expect that for low T_c materials, a faster decrease of $M(T)$ shows up at a lower T or I_p , where the QSS effect on f_r is comparatively weaker. The Ni can be a good tester to examine the competition of the thermal and strain effects. The Ni has low values of $T_c = 630$ K and $M = 525$ emu cm⁻³ which are the key parameters for enhancing the thermal effect, but similar λ_s, β , and B values to Co which are related to the strain effect. Figure 3c shows the contour map of f_r including the QSS effect for Ni, and Fig. 3d presents $\Delta f/f_m$ for $\varphi = 25, 45$, and 60° selected from the contour map. In contrast to the Co case, f_r decreases first at a low T , meaning that the thermal effect is dominant, and is switched to the increase with increasing

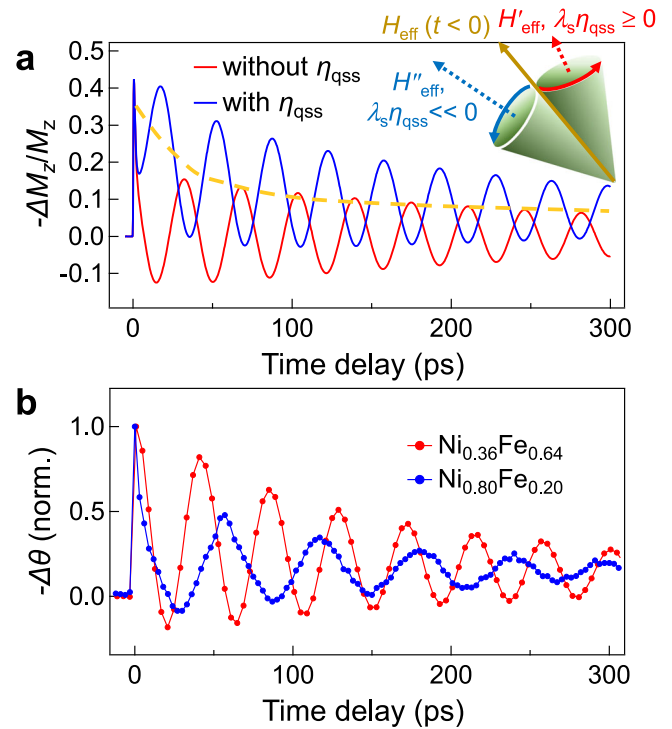


Fig. 4 Quasi-static strain (QSS) effect governing spin dynamics. a Calculated curves of spin dynamics based on the Landau-Lifshitz-Gilbert (LLG) equation for the absence (red) and presence (blue curve) of η_{QSS} under $H_{\text{ext}} = 0.54$ T and $\varphi = 60^\circ$. The π -phase inversion is clearly observed around 20 ps. The yellow dashed curve marks the monotonic-decaying background originated by a coherent rotation of $H_{\text{eff}}(t)$ to the in-plane direction. Inset: schematic diagram describing the rotation direction of $H_{\text{eff}}(t)$ depending on either QSS (blue) or thermal effect (red). b Experimental verification of the π -phase inversion of the spin precession for materials with negligible magnetoelastic energy (Ni_{0.36}Fe_{0.64} (red): the thermal expansion coefficient $\beta \sim 0$, Ni_{0.80}Fe_{0.20} (blue circles): the magnetostriction value $\lambda_s \sim 0$).

T . To prove those results experimentally, $\Delta\theta(t)$ of Ni(270)/SiO₂ at $\varphi = 25^\circ$ and $I_p \leq 2.2$ mJ cm⁻² was measured and plotted in Fig. 3e. As presented in the inset, after fitting the data with Eq. (1) (denoted as the solid line for the highest I_p), $\Delta f/f_m$ becomes first negative and then positive as I_p increases (the error bars are marked on the data points). These curves reproduce the calculation (Fig. 3d) in excellent agreement supporting our analysis on thermal and QSS effects.

Governing role of QSS on ultrafast spin dynamics. We address that the QSS has a decisive role in determining the initial status of spin dynamics judged by further features that have been under-rated. The first point is the phase of the spin precession. Figure 4a presents the calculated curves of $\Delta M_z(t)/M_z$ for the absence (red) and presence (blue curve) of $\eta_{\text{QSS}}(z, t)$ under $H_{\text{ext}} = 0.54$ T and $\varphi = 60^\circ$. Here the spin precessions in Co and Ni (Figs. 2a and 3e) correspond to the blue curve, leading to a π -phase inversion compared to conventional free energy analysis.

The pictorial description of the inset explains the π -phase difference concisely. According to conventional energy analysis, the sudden decrease in $M(t)$ after photo-excitation results in a rotation of $H_{\text{eff}}(t)$ (yellow solid arrow) to the out-of-plane direction ($H'_{\text{eff}}(t)$ —red dashed arrow) due mainly to the decrease in dipolar energy (for polycrystalline or isotropic materials) and starts precessing around the new axis $H'_{\text{eff}}(t)$. This aspect takes place when the thermal effect dominates the QSS effect for such conditions of $\lambda_s \eta_{\text{QSS}} \geq 0$ ($\lambda_s \geq 0, \beta \geq 0$ or $\lambda_s \leq 0, \beta \leq 0$) and even

$\lambda_s \eta_{\text{QSS}} \leq 0$ ($\lambda_s \leq 0, \beta \geq 0$) provided the magnitude of λ_s is small. On the other hand, for $\lambda_s \eta_{\text{QSS}} \ll 0$, the QSS effect prevails over the thermal effect and drives the rotation of $H_{\text{eff}}(t)$ towards the in-plane direction ($H'_{\text{eff}}(t)$ —blue dashed arrow). Then, the spins start the precession around the $H'_{\text{eff}}(t)$ axis. This orientation is determined at the initial stage of the precession, immediately after demagnetization. $\text{Ni}_x\text{Fe}_{1-x}(180)/\text{Al}_2\text{O}_3$ films were tested experimentally to verify this scenario, as plotted in Fig. 4b. As the alloys of $x \sim 0.36$ and 0.8 have negligible β and λ_s values, respectively, it is expected that they have low magnetoelastic energy ($\propto \lambda_s \beta \Delta T$). These cases rotate $H_{\text{eff}}(t)$ towards $H'_{\text{eff}}(t)$, inducing negative values of signals at the first half period (20–30 ps) as the conventional analysis does, as shown with the red graph in Fig. 4a.

The second feature is the pronounced decaying background (yellow dashed line in Fig. 4a). This in general has been considered as incoherent thermal phonons and magnons with nonzero wavenumbers³⁸, which have the heat dissipation timescale. Rather, our analysis suggests that this needs to be interpreted as the contribution of coherent rotation of $H_{\text{eff}}(t)$ because of the QSS effect. This was clearly verified from the fact that Co and Ni with high magnetoelastic energy have much larger decaying offsets than those of NiFe alloys. These all features mentioned above, including the frequency increase in the spin precession, are reproduced through the model calculation incorporating only one concept of the QSS effect with the full consistency with the experimental data.

Discussion

By decoupling the thermal and the QSS effects using USI and the MOKE, we proved that the QSS has a governing role over the thermal effect on the overall behavior of ultrafast spin dynamics over a wide range of time scales. The ultrafast photo-excitation can strengthen the effective magnetic field due to the QSS effect. This leads to a higher frequency of spin precession and accounts for the π -phase inversion determined from the initial stage of the precession. Besides, the long-lived offset with the relaxation timescale of the QSS was interpreted as extra gain induced by the contribution of a coherent rotation of $H_{\text{eff}}(t)$. This study shows that the QSS is involved universally in a wide family of magnetoelastic materials and should be treated fundamentally.

The strain of 0.1–1% generated by photo-excitation is high enough to induce the modification of the electronic band structure²⁶ even at ultrafast time scales³⁹. Therefore, it can be predicted that the QSS modifies the dielectric tensors bringing about features such as derivative-like changes in differential magneto-optics. And this will lead to inequivalence between its real and imaginary parts of magneto-optic signal, and involuntary extra gains in differential reflectivity as well even after thermal equilibrium timescale. To date, considerable effort has been made to identify genuine magnetism and the origin of demagnetization^{3,20,40–46}. Our demonstration that the QSS governs the spin dynamics provides an interpretation of ultrafast magneto-optics and therefore helps to better understand the physical mechanisms behind ultrafast phenomena by considering both strain and thermal effects.

Methods

Time-resolved pump-probe MOKE. We used Ti:sapphire regenerative amplified laser pulses with a repetition rate of 10 kHz, a temporal width of 40 fs, and a center wavelength of 800 nm. The pump pulses are frequency-doubled with a beta Barium Borate crystal and have a temporal width of 60 fs at a sample position. The pump and probe pulses were focused on the sample with diameter sizes of 150 and 30 μm , respectively, and their intensity ratio was set to $\sim 1000:1$. The reflected probe pulses from the samples were split into orthogonal polarizations using a Wollaston prism and analyzed into the differential Kerr rotation $\Delta\theta(t)$ and differential reflectivity $\Delta R(t)$. An external magnetic field of $H_{\text{ext}} = 0.4$ T was applied with various angles φ from the normal to the sample plane.

Ultrafast Sagnac interferometer. An ultrafast Sagnac interferometer based on a Ti:sapphire oscillator system issued with a center wavelength of 800 nm and a temporal width of 40 fs was employed to obtain a quantitative profile of the time-resolved lattice thermal expansion after the pump excitation. After passing through an electro-optic modulator operating at 1 MHz, the dispersed pulse was compressed to 45 fs by pairs of negative-chirped mirrors. The pump pulses were frequency-doubled by a 500- μm -thick BiB_3O_6 crystal with a conversion efficiency of 25% and had a temporal width of 65 fs at a sample position. The probe and pump pulses were focused on the front and back sides of the samples in normal incidence. The numerical apertures of the objective lenses used in each beam line were 0.55 and 0.4, respectively. The temporal delay between p-pol. (arrives at a negative delay) and s-pol. probes (arrives at a positive delay) at the sample position were fixed to ~ 1 ns and the s-pol. probes measure the pump-induced optical responses (ρ and $d\phi$) (Supplementary Note 1 for more details of the setup schematics and characteristics).

Strain calculation and parameter values. To obtain $\eta(z, t)$, it is necessary to solve the three temperatures model and one-dimensional wave equation in the $\text{Co}(25)/\text{Al}_2\text{O}_3$ structure. The three temperatures model (Eq. (5)) is described as follows:

$$C_i(T_i) \frac{\partial T_i}{\partial t} = \delta_{ie} \left[\frac{\partial}{\partial z} \left(\kappa \frac{\partial T_i}{\partial z} \right) + P(z, t) \right] - g_{ij} \Delta T_{ij} \quad (5)$$

where $i, j = e, l, s$ stand for electrons, lattice, and spins, respectively. The C_i and κ are the heat capacity per unit volume of bath i and the thermal conductivity. The g_{ij} is the coupling coefficient between two baths i and j , and $P(z, t)$ the laser source term. The ΔT_{ij} is defined as $T_i - T_j$, the temperature difference between two baths i and j . Using boundary conditions—continuities of both the heat transfer at air/Co ($0 = \kappa_{\text{Co}} \frac{\partial T_e}{\partial z} |_{z=0, \text{Co}}$), Co/ Al_2O_3 ($\kappa_{\text{Co}} \frac{\partial T_e}{\partial z} |_{z=d, \text{Co}} = \kappa_{\text{Al}_2\text{O}_3} \frac{\partial T_l}{\partial z} |_{z=d, \text{Al}_2\text{O}_3}$) and the temperatures at Co/ Al_2O_3 ($T_e(z, t) |_{z=d, \text{Co}} = T_{\text{Al}_2\text{O}_3}(z, t) |_{z=d, \text{Al}_2\text{O}_3}$)—temperature profiles of the three baths were obtained (d is a film thickness). Here, since there is an arbitrariness for the selection of pump intensity and unknown value of C_s , we carefully chose the value by matching with the experimental data of both $u(z=0, t)$ of the Sagnac measurement and the demagnetization $\Delta\theta_l(t)/\theta_l$ (longitudinal Kerr geometry) under $H_{\text{ext}} = 0.5$ T and $\varphi = 90^\circ$. That is, $T_l(z, t)$ obtained from three temperature models calculation (Eq. (5)) is linked to $u(z, t)$ through the one-dimensional wave equation (Eq. (6)) as follows:

$$\frac{\partial^2 u(z, t)}{\partial t^2} = v^2 \frac{\partial^2 u(z, t)}{\partial z^2} - \frac{3\beta B \partial T_l}{\rho \partial z} \quad (6)$$

where ρ is the mass density, v the sound velocity, β the linear thermal expansion coefficient, and B the bulk modulus. Using boundary conditions, continuities of both the stress at air/Co ($3 \frac{1-\nu}{1+\nu} B \frac{\partial u}{\partial z} = 3\beta B \Delta T_l$), Co/ Al_2O_3 ($3 \frac{1-\nu}{1+\nu} B \frac{\partial u}{\partial z} - 3\beta B \Delta T_l = 3 \frac{1-\nu_{\text{Al}_2\text{O}_3}}{1+\nu_{\text{Al}_2\text{O}_3}} B_{\text{Al}_2\text{O}_3} \frac{\partial u}{\partial z}$), and the displacements at Co/ Al_2O_3 ($u(z, t) |_{z=d, \text{Co}} = u(z, t) |_{z=d, \text{Al}_2\text{O}_3}$)— $u(z, t)$ were solved. Then, $\eta_{\text{QSS}}(t) = \partial u(z, t) / \partial z |_{z=0}$ was determined by matching $u(0, t)$ with the Sagnac measurement curve, as shown in Fig. 1c. The parameter values used in the simulation are as follows: $C_e = 6.6 \times 10^2 T_e$, $C_l = 3.5 \times 10^6$ ⁴⁷, $C_s = -W_m dM^2/dT_s \text{ J m}^{-3} \text{ K}^{-1}$ ⁴⁸ where a molecular field prefactor W_m was assumed to be 4.5×10^8 for Co, and $C_l = 3.1 \times 10^6$ for Al_2O_3 ⁴⁹. $\kappa_{\text{Co}} = 64$ ⁴⁷, $\kappa_{\text{Al}_2\text{O}_3} = 20 \text{ W m}^{-1} \text{ K}^{-1}$ ⁵⁰ at 500 K, $B = 190$ GPa, $\nu = 0.31$ for Co²⁷. For dynamic heat coupling coefficients between two sub-systems, we used the following values: $g_{el} = 1.3 \times 10^{18}$, $g_{ls} = 5.0 \times 10^{17}$, and $g_{es} = 3.5 \times 10^{17} \text{ W m}^{-3} \text{ K}^{-1}$ to match with the $\Delta\theta_l(t)/\theta_l$ and $u(0, t)$ curves qualitatively. For the Curie–Weiss curve, $M(T) = M_s(1 - 1.058(T/T_c)^\alpha)^\zeta$ was extracted by fitting the data in ref. ⁵¹, here $M_s = 1360 \text{ emu cm}^{-3}$, $T_c = 1380$ K, $\alpha = 3.15$, and $\zeta = 0.50$.

Data availability

The data that support the findings of this study are available from the authors upon reasonable request.

Received: 1 August 2021; Accepted: 22 February 2022;

Published online: 14 March 2022

References

- Kittel, C. Interaction of spin waves and ultrasonic waves in ferromagnetic crystals. *Phys. Rev.* **110**, 836–841 (1958).
- Beaurepaire, E., Merle, J.-C., Daunois, A. & Bigot, J.-Y. Ultrafast spin dynamics in ferromagnetic nickel. *Phys. Rev. Lett.* **76**, 4250–4253 (1996).
- Koopmans, B., van Kampen, M., Kohlhepp, J. T. & de Jonge, W. J. M. Ultrafast magneto-optics in nickel: magnetism or optics? *Phys. Rev. Lett.* **85**, 844–847 (2000).
- Zhang, G. P. & Hübner, W. Laser-induced ultrafast demagnetization in ferromagnetic metals. *Phys. Rev. Lett.* **85**, 3025–3028 (2000).
- Kirilyuk, A., Kimel, A. V. & Rasing, T. Ultrafast optical manipulation of magnetic order. *Rev. Mod. Phys.* **82**, 2731–2784 (2010).

6. Hofherr, M. et al. Ultrafast optically induced spin transfer in ferromagnetic alloys. *Sci. Adv.* **6**, eaay8717 (2020).
7. Gort, R. et al. Early stages of ultrafast spin dynamics in a 3D ferromagnet. *Phys. Rev. Lett.* **121**, 087206 (2018).
8. Bigot, J.-Y., Vomir, M., Andrade, L. H. F. & Beaurepaire, E. Ultrafast magnetization dynamics in ferromagnetic cobalt: the role of the anisotropy. *Chem. Phys.* **318**, 137–146 (2005).
9. Hohlfeld, J. et al. Fast magnetization reversal of GdFeCo induced by femtosecond laser pulses. *Phys. Rev. B* **65**, 012413 (2001).
10. Radu, I. et al. Transient ferromagnetic-like state mediating ultrafast reversal of antiferromagnetically coupled spins. *Nature* **472**, 205–208 (2011).
11. Mathias, S. et al. Probing the timescale of the exchange interaction in a ferromagnetic alloy. *Proc. Natl Acad. Sci. USA* **109**, 4792–4797 (2012).
12. Batignani, G. et al. Probing ultrafast photo-induced dynamics of the exchange energy in a Heisenberg antiferromagnet. *Nat. Photon* **9**, 506–510 (2015).
13. Kampfrath, T. et al. Coherent terahertz control of antiferromagnetic spin waves. *Nat. Photon* **5**, 31–34 (2011).
14. Baiert, S. et al. Nonlinear spin control by terahertz-driven anisotropy fields. *Nat. Photon* **10**, 715–718 (2016).
15. Scherbakov, A. V. et al. Coherent magnetization precession in ferromagnetic (Ga,Mn)As induced by picosecond acoustic pulses. *Phys. Rev. Lett.* **105**, 117204 (2010).
16. Kim, J.-W., Vomir, M. & Bigot, J.-Y. Ultrafast magnetoacoustics in nickel films. *Phys. Rev. Lett.* **109**, 166601 (2012).
17. Némec, P. et al. Experimental observation of the optical spin transfer torque. *Nat. Phys.* **8**, 411–415 (2012).
18. Huisman, T. J. et al. Femtosecond control of electric currents in metallic ferromagnetic heterostructures. *Nat. Nanotechnol.* **11**, 455–458 (2016).
19. Choi, G.-M. et al. Optical spin-orbit torque in heavy metal-ferromagnet heterostructures. *Nat. Commun.* **11**, 1482 (2020).
20. Dornes, C. et al. The ultrafast Einstein–de Haas effect. *Nature* **565**, 209–212 (2019).
21. Kovalenko, O., Pezeril, T. & Temnov, V. V. New concept for magnetization switching by ultrafast acoustic pulses. *Phys. Rev. Lett.* **110**, 266602 (2013).
22. Janušonis, J. et al. Ultrafast magnetoelastic probing of surface acoustic transients. *Phys. Rev. B* **94**, 024415 (2016).
23. Thevenard, L. et al. Precessional magnetization switching by a surface acoustic wave. *Phys. Rev. B* **93**, 134430 (2016).
24. Kats, V. N. et al. Ultrafast changes of magnetic anisotropy driven by laser-generated coherent and noncoherent phonons in metallic films. *Phys. Rev. B* **93**, 214422 (2016).
25. Kim, J.-W., Kovalenko, O., Liu, Y. & Bigot, J.-Y. Exploring the Angstrom excursion of Au nanoparticles excited away from a metal surface by an impulsive acoustic perturbation. *ACS Nano* **10**, 10880–10886 (2016).
26. Akimov, A. V., Scherbakov, A. V., Yakovlev, D. R., Foxon, C. T. & Bayer, M. Ultrafast band-gap shift induced by a strain pulse in semiconductor heterostructures. *Phys. Rev. Lett.* **97**, 037401 (2006).
27. Rao, R. R. & Ramanand, A. Thermal expansion and bulk modulus of cobalt. *J. Low. Temp. Phys.* **26**, 365–377 (1977).
28. Aggarwal, R. L. & Ramdas, A. K. *Physical Properties of Diamond and Sapphire* (CRC, 2019).
29. Tachizaki, T. et al. Scanning ultrafast Sagnac interferometry for imaging two-dimensional surface wave propagation. *Rev. Sci. Instrum.* **77**, 043713 (2006).
30. Saito, T., Matsuda, O. & Wright, O. B. Picosecond acoustic phonon pulse generation in nickel and chromium. *Phys. Rev. B* **67**, 205421 (2003).
31. Pezeril, T. et al. Femtosecond imaging of nonlinear acoustics in gold. *Opt. Express* **22**, 4590–4598 (2014).
32. Wright, O. B. Ultrafast nonequilibrium stress generation in gold and silver. *Phys. Rev. B* **49**, 9985–9988 (1994).
33. Reid, A. H. et al. Beyond a phenomenological description of magnetostriction. *Nat. Commun.* **9**, 388 (2018).
34. von Reppert, A. et al. Spin stress contribution to the lattice dynamics of FePt. *Sci. Adv.* **6**, eaba1142 (2020).
35. von Reppert, A. et al. Ultrafast laser generated strain in granular and continuous FePt thin films. *Appl. Phys. Lett.* **113**, 123101 (2018).
36. Scott, G. G. Gyromagnetic ratio of cobalt. *Phys. Rev.* **104**, 1497–1498 (1956).
37. Kloholm, E. & Aboaf, J. The saturation magnetostriction of thin polycrystalline films of iron, cobalt, and nickel. *J. Appl. Phys.* **53**, 2661–2663 (1982).
38. Djordjevic, M. et al. Comprehensive view on ultrafast dynamics of ferromagnetic films. *Phys. Status Solidi C* **3**, 1347–1358 (2006).
39. Pudell, J. et al. Layer specific observation of slow thermal equilibration in ultrathin metallic nanostructures by femtosecond X-ray diffraction. *Nat. Commun.* **9**, 3335 (2016).
40. Bigot, J.-Y., Guidoni, L., Beaurepaire, E. & Saeta, P. N. Femtosecond spectrotemporal magneto-optics. *Phys. Rev. Lett.* **93**, 077401 (2004).
41. Bigot, J.-Y., Vomir, M. & Beaurepaire, E. Coherent ultrafast magnetism induced by femtosecond laser pulses. *Nat. Phys.* **5**, 515–520 (2009).
42. Battiato, M., Carva, K. & Oppeneer, P. M. Superdiffusive spin transport as a mechanism of ultrafast demagnetization. *Phys. Rev. Lett.* **105**, 027203 (2010).
43. Radu, I. et al. Laser-induced magnetization dynamics of lanthanide-doped permalloy thin films. *Phys. Rev. Lett.* **102**, 117201 (2009).
44. Zhang, G. P., Hübner, W., Lefkidis, G., Bai, Y. & George, T. F. Paradigm of the time-resolved magneto-optical Kerr effect for femtosecond magnetism. *Nat. Phys.* **1315**, 499–502 (2009).
45. Koopmans, B. et al. Explaining the paradoxical diversity of ultrafast laser-induced demagnetization. *Nat. Mater.* **9**, 259–265 (2010).
46. Siegrist, F. et al. Light-wave dynamic control of magnetism. *Nature* **571**, 240–244 (2019).
47. Montague, S. A., Draper, C. W. & Rosenblatt, G. M. Thermal diffusivities of hafnium and cobalt from 300 to 1000K. *J. Phys. Chem. Solid* **40**, 987–992 (1979).
48. Morrish, A. H. *The Physical Principles of Magnetism* 259–275 (Wiley-IEEE, 2001).
49. Xu, Y., Wang, H., Tanaka, Y., Shimono, M. & Yamazaki, M. Measurement of interfacial thermal resistance by periodic heating and a thermo-reflectance technique. *Mater. Trans.* **48**, 148–150 (2007).
50. Cahill, D. G., Lee, S.-M. & Selinder, T. I. Thermal conductivity of κ -Al₂O₃ and α -Al₂O₃ wear-resistant coatings. *J. Appl. Phys.* **83**, 5783–5786 (1998).
51. Stiffler, W. W. The magnetization of cobalt as a function of the temperature and the determination of its intrinsic magnetic field. *Phys. Rev. (Ser. I)* **33**, 268–294 (1911).

Acknowledgements

We gratefully thank G. Versini at IPCMS in CNRS for his effort to grow good-quality samples. J.-W.K. acknowledges support from Basic Science Research Program through the National Research Foundation of Korea (NRF) funded by the Ministry of Education (2017R1A6A3A04011173) and by the MSIT (2021R1A4A1031920). Y.S. acknowledges support from the Basic Science Research Program through the National Research Foundation of Korea (NRF) funded by the Ministry of Education (2020R111A1A101075040). D.-H.K. acknowledges support from Korea Research Foundation (NRF) (2018R1A2B3009569 and 2020R1A4A1019566). J.-R.J. acknowledges support from the National Research Foundation of Korea (NRF) grant funded by the Korean government (MSIT) (2020R1A2C100613611) and M.V. acknowledges support from the Agence Nationale de la Recherche in France via the project EquipEx UNION No. ANR-10-EQPX-52.

Author contributions

J.-W.K. conceived the experiment. J.-W.K. and Y.S. prepared TR-MOKE and Sagnac interferometer data. J.-R.J. and P.C.V. fabricated NiFe alloy films. J.-W.K. performed data analysis and simulation with the help of Y.S. J.-W.K. wrote the manuscript with the help of M.V. and D.-H.K. All authors discussed the results and commented on the manuscript.

Competing interests

The authors declare no competing interests.

Additional information

Supplementary information The online version contains supplementary material available at <https://doi.org/10.1038/s42005-022-00836-z>.

Correspondence and requests for materials should be addressed to Ji-Wan Kim.

Peer review information *Communications Physics* thanks the anonymous reviewers for their contribution to the peer review of this work. Peer reviewer reports are available.

Reprints and permission information is available at <http://www.nature.com/reprints>

Publisher's note Springer Nature remains neutral with regard to jurisdictional claims in published maps and institutional affiliations.

 **Open Access** This article is licensed under a Creative Commons Attribution 4.0 International License, which permits use, sharing, adaptation, distribution and reproduction in any medium or format, as long as you give appropriate credit to the original author(s) and the source, provide a link to the Creative Commons license, and indicate if changes were made. The images or other third party material in this article are included in the article's Creative Commons license, unless indicated otherwise in a credit line to the material. If material is not included in the article's Creative Commons license and your intended use is not permitted by statutory regulation or exceeds the permitted use, you will need to obtain permission directly from the copyright holder. To view a copy of this license, visit <http://creativecommons.org/licenses/by/4.0/>.

© The Author(s) 2022